

Strong spin-orbit interactions in a correlated two-dimensional electron system formed in SrTiO₃(001) films grown epitaxially on *p*-Si(001)

Ryan J. Cottier, Barry D. Koehne , John T. Miracle , Daniel A. Currie, and Nikoleta Theodoropoulou ^{*}
Department of Physics, Texas State University, San Marcos, Texas 78666, USA

Leonidas Pantelidis
Department of Physics & Astronomy, Hanover College, Hanover, Indiana 47243, USA

Andrei Hernandez-Robles  and Arturo Ponce 
Department of Physics & Astronomy, University of Texas at San Antonio, One UTSA Circle, San Antonio Texas 78249, USA

 (Received 8 October 2019; revised 30 July 2020; accepted 28 August 2020; published 18 September 2020)

We observe strong spin-orbit interactions in a two-dimensional electron system formed on SrTiO₃(001) films grown epitaxially on *p*-Si(001). High-resolution transmission electron microscopy and related analytical techniques reveal a sharp interface between Si and SrTiO₃. Strain mapping analysis shows in-plane strain in SrTiO₃ very close to the interface. Analysis of the low temperature magnetoconductance measurements reveals that both quantum interference and electron-electron interactions are important. The contributions of these two quantum phenomena to the temperature and magnetic field dependence of the conductance and Hall effect are separated. The electron system has carrier concentrations larger than 10^{14}cm^{-2} , appears to be confined within ~ 4 nm, and has an estimated spin-splitting energy ~ 12 meV.

DOI: [10.1103/PhysRevB.102.125423](https://doi.org/10.1103/PhysRevB.102.125423)

I. INTRODUCTION

Manipulating the spin of electrons by controlling their motion via applied electric fields in zero magnetic field is possible if spin-orbit coupling is strong. This has been a long-standing goal for devices with applications in spintronics and quantum computing. Spin-orbit coupling can be caused by interface inversion asymmetry associated with the chemical bonding within interfaces and by inversion asymmetry of the potentials including a built-in electric field or an external gate-voltage [1]. Strain can also induce inversion asymmetry and lead to spin-orbit coupling; 0.2% strain has been shown to strengthen spin-orbit interactions (SOI) by as much as 20% [2]. In oxide systems, SOI are predicted to be very sensitive to local polarizations tending to be stronger in easily polarizable materials such as SrTiO₃. Polar lattice displacements between oxygen and metal break the reflection symmetry in the *xy* plane producing a Rashba effect while the SOI strength can be controlled by the bond angles between oxygen and metals [3,4]. Large Rashba spin splitting induced by polarization is also predicted for compressively strained SrTiO₃ thin films [5].

Spin-orbit coupling has been demonstrated in two-dimensional electron systems (2DES) formed at the interface between LaAlO₃ and SrTiO₃ and also at the surface of SrTiO₃ under field gating [6,7]. The consensus so far is that field gating allows for tuning the carrier concentration of the 2DES

in SrTiO₃-based systems by band filling and spin-orbit coupling is realized due to a multiband effect. The conduction band of SrTiO₃ originates from Ti 3*d* *t*_{2*g*} bands. Quantum confinement at a conducting (001) SrTiO₃ surface lifts the degeneracy between the *t*_{2*g*} orbitals due to band bending. The splitting between the lowest energy *d*_{*xy*} band and the *d*_{*yz*}/*d*_{*zx*} bands at the Γ point can be ~ 300 meV [8] depending on the confinement potential. Most electrons occupy the light *d*_{*xy*} band and are confined in the *xy* plane near the surface [9,10] while carriers in the heavy *d*_{*zx*}/*d*_{*yz*} bands extend further away from the interface [11]. Spin splitting of ~ 10 meV occurs at the anticrossing region of the *d*_{*xy*} and *d*_{*yz*}/*d*_{*zx*} bands due to multiorbital effects [8,12,13] and can be predominantly cubic in the wave vector *k* [13,14].

In this letter, we show that spin-orbit coupling and quantum confinement are also present in a 2DES formed on SrTiO₃ thin films. The oxide films are epitaxially grown on a *p*-Si (001) substrate, the workhorse of semiconductor industry, thus providing a direct route for the realization of SOI-based devices on Si with potential technological impact. Moreover, the 2DES has high electron carrier concentrations $\sim 10^{14}\text{cm}^{-2}$ that occur spontaneously (without gating), appears to be confined within 4 nm, and its estimated spin splitting energy exceeds 12 meV. Electron-electron interactions (EEI) also play an important role in the magnetotransport behavior and together with quantum interference entirely determine the temperature and magnetic field dependence of the conductivity and Hall resistance. Transmission electron microscopy (TEM) shows a chemically abrupt interface and heteroepitaxy while strain analysis reveals in-plane strain at the interface due to the heteroepitaxy as expected.

^{*}ntheo@txstate.edu

SrTiO₃ on Si was originally proposed as an alternative gate dielectric on Si because of its very high dielectric constant. Until recently, SrTiO₃/Si was believed to form a type-II heterojunction with a very small conduction band offset [15] hence making it an incompatible gate dielectric for Complementary Metal Oxide Semiconductor (CMOS) applications. However, recent reports show that SrTiO₃ band bending at the interface with Si creates a potential well of ~ 2 V confining the carriers to a few nanometers in the out-of-plane direction and a high-density electron gas was predicted to arise near the interface [16].

Highly crystalline SrTiO₃ films can be grown directly on Si by oxide Molecular Beam Epitaxy (MBE). SrTiO₃ grows coherently on Si(001) by a 45° rotation around the surface normal [17]. Due to the lattice mismatch, the SrTiO₃ unit cell is tetragonally distorted; it is biaxially compressed in-plane by 1.7% and extended along the growth direction [18–20]. Formation of an interfacial oxide layer (SiO₂) is suppressed at low O₂ pressures producing a sharp interface with SrTiO₃. Low O₂ pressure also causes oxygen-deficient films. Epitaxial SrTiO₃ films on (001) Si substrates deposited by MBE can be commensurately strained to Si (001) [21] up to a critical thickness of ~ 2 nm after which plastic deformation occurs through the formation of dislocations [21,22].

We employ low temperature magnetotransport measurements to investigate the electronic properties of the 2DES at the SrTiO₃/Si(001) heterojunction. SOI are manifested through weak antilocalization (WAL) effects. The conductivity of low-dimensional structures at low temperatures is largely determined by quantum effects. The two physical mechanisms that lead to quantum corrections to the classical Drude conductivity σ_D are the weak localization (WL) or interference effects [23], and EEI [24]. In 2D, both corrections are logarithmic in temperature [24] in the diffusive regime $\frac{k_B T \tau}{\hbar} \ll 1$, where τ is the elastic scattering time, T is the temperature, k_B is Boltzmann's constant, and \hbar is Planck's constant divided by 2π . The conductivity correction due to interference effects is $\delta\sigma_{WL}(T) = G_0 \ln\left(\frac{\tau}{\tau_\phi}\right)$, when $\tau_\phi \approx \tau_{so}$ where $G_0 = e^2/\pi h = 1.23 \times 10^{-5} S$, e the electronic charge, τ_ϕ is the phase coherence time, the time in which phase information is lost by a carrier, and τ_{so} is the spin-relaxation time. For EEI effects,

$$\delta\sigma_{EEI}(T) = G_0 K_{ee} \ln\left(\frac{k_B T \tau}{\hbar}\right), \quad (1)$$

where $K_{ee} = 1 + 3\left(1 - \frac{\ln(1+F_0^\sigma)}{F_0^\sigma}\right)$, and $F_0^\sigma < 0$ is the interaction constant in the triplet channel [24].

If the main source of dephasing is Coulomb interactions, $\tau_\phi \propto T^{-1}$, $\delta\sigma_{WL} < 0$, and the total conductivity correction (up to a temperature-independent term) is $\delta\sigma(T) = G_0(1 + K_{ee})\ln\left(\frac{k_B T \tau}{\hbar}\right)$. The measured conductivity is $\sigma(T) = \sigma_D + \delta\sigma(T)$, with $\sigma = 1/R_s$ and $\sigma_D = en_s \mu = \frac{e^2 n_s \tau}{m^*}$, where R_s is the sheet resistance, n_s the sheet carrier concentration, μ the mobility, and m^* is the effective mass. We use $m^* = 1.2m_e$ [25,26]. In 3D, the quantum corrections to conductivity are $\frac{\delta\sigma_{3d}^{EEI}(T)}{G_0} = a\sqrt{\frac{k_B T}{\hbar D}}$ and $\frac{\delta\sigma_{3d}^{WL}(T)}{G_0} = (T/T_0)^{p/2}$ where the coefficient a depends on the interaction constant and $p > 1$ ($p = 2$ for Coulomb interactions and $p = 3$ for electron-phonon scattering) [24,27]. At the lowest temperatures ($\frac{k_B T}{\hbar D}, \frac{T}{T_0} < 1$), the

interaction term which has a \sqrt{T} dependence dominates the 3D conductivity correction [27].

A perpendicular magnetic field B suppresses the electronic phase coherence and in the diffusive limit, the magnetoconductance (MC) is given by the Iordanskii-(Lyanda-Geller)-Pikus (ILP) model [28]. When the linear Rashba contribution is negligible as in the case for SrTiO₃-based systems due to the $m_j = 3/2$ character of the d_{xy} orbital [7,29], ILP reduces to the Hikami-Larkin-Nagaoka (HLN) expression:

$$\begin{aligned} MC_{WAL} &= \frac{\Delta\sigma_{WAL}}{G_0} \\ &= \psi\left(\frac{1}{2} + \frac{B_\phi + B_{so}}{B}\right) + \frac{1}{2}\psi\left(\frac{1}{2} + \frac{B_\phi + 2B_{so}}{B}\right) \\ &\quad - \frac{1}{2}\psi\left(\frac{1}{2} + \frac{B_\phi}{B}\right) - \ln\frac{B_\phi + B_{so}}{B} \\ &\quad - \frac{1}{2}\ln\left(\frac{B_\phi + 2B_{so}}{B}\right) + \frac{1}{2}\ln\left(\frac{B_\phi}{B}\right), \end{aligned}$$

where ψ is the digamma function and the two fitting parameters are B_ϕ and B_{so} , with $B_{\phi,so} = \frac{\hbar}{4el_{\phi,so}^2}$, $l_{\phi,so}^2 = \mathcal{D}\tau_{\phi,so}$, where $l_{\phi,so}$ are the respective phase-coherence and spin-relaxation lengths, $\mathcal{D} = \frac{1}{2}u_F^2\tau$ is the diffusion transport coefficient in 2D, $u_F = \hbar k_F/m^*$ is the Fermi velocity, k_F is the Fermi quasimomentum. The HLN expression is valid in the diffusive with respect to the magnetic field regime, $B < B_{tr} = \frac{\hbar}{4e\mathcal{D}\tau}$ and can also describe the MC of systems with an arbitrarily complex Fermi surface or multiband systems [30]. If delocalized electrons contribute to transport, the MC includes an additional term which accounts for the classical orbital magnetoresistance (Kohler term): $MC_{Khl} = \Delta\sigma_{Khl}/G_0 = -A_K \frac{B^2}{1+m^2 B^2}$, where A_K and m are temperature-dependent parameters. The EEI correction in the longitudinal resistivity is independent of the magnetic field unless the Zeeman energy is greater than the thermal energy [31–33]. Finally, quantum interference effects and SOI should not affect the transverse magnetoresistance R_{xy} , while EEI modify the Hall coefficient $R_H = R_{xy}/B$ by $(\delta R_H)_{EEI}$ so that $\frac{(\delta R_H)_{EEI}}{R_H} = -2\frac{\delta\sigma_{EEI}}{\sigma_D}$ as $T \rightarrow 0$ [24].

II. EXPERIMENTAL DETAILS

SrTiO₃ films were grown on *p*-Si(001) (Boron doped, $\sim 5 \times 10^{15} \text{ cm}^{-3}$) by oxide-MBE using Ti and Sr effusion cells for codeposition at a base pressure of 5×10^{-10} Torr [34]. The O₂ partial pressure was maintained at 4×10^{-8} Torr during the entire growth. The surface quality and stoichiometry were monitored continuously using *in situ* reflection high-energy electron diffraction. Substrate oxidation was avoided using the growth procedure described in Ref. [34]. The samples were Ti terminated. To preserve the strain, maintain a pristine interface, and prevent diffusion of oxygen vacancies, the films were not annealed postdeposition. The temperature and magnetic field dependence of the resistance was measured using a standard four-point dc technique in the Van der Pauw configuration with Cr [35] or Al [36] Ohmic contacts deposited through a shadow mask. All transport measurements were reproducible over several months and no hysteresis or

irreversibility was observed. We report low-temperature magnetotransport results on two heterojunctions with $d = 20$ nm (film A) and $d = 60$ nm (film B) grown on semi-insulating Si(001) substrates [37], where d is the thickness of the SrTiO₃ layer. These two films have similar sheet resistance and slightly different sheet carrier concentrations. The 60-nm sample was also imaged by TEM using a JEOL ARM 200F operated at 200 kV; the sample was prepared for cross-section view using mechanical polishing followed by Ar⁺ ion milling.

III. RESULTS AND DISCUSSIONS

High resolution TEM (HRTEM) [Fig. 1(a)] and selected area electron diffraction (SAED) pattern [Fig. 1(b)] show the epitaxial quality of the 60-nm film. The superimposed SAED patterns show the epitaxial growth and the 45° in-plane rotational offset with an epitaxial orientation relationship SrTiO₃ [100]//Si[110] zone axes [21]. The orientation relationship between SrTiO₃ (STO) and Si in the diffraction pattern is measured by selecting the in-plane reflections

$(g_{2\bar{2}0})_{\text{Si}}$ and $(g_{200})_{\text{STO}}$ and is showing a $\sim 1.6\%$ lattice mismatch between Si and SrTiO₃, as expected. Additionally, energy-dispersive x-ray spectroscopy (EDS) was performed using aberration-corrected scanning transmission electron microscopy (Cs-STEM) with the high angle annular dark field detector (HAADF) [Fig. 1(c)]. The integrated EDS spectrum [Fig. 1(d)] is aligned with the HAADF-STEM image of Fig. 1(c). Below the interface only silicon is detected and above the interface, Ti, O, and Sr, the SrTiO₃ elements, are detected, showing clearly the abrupt chemical interface between Si and SrTiO₃. Since EDS energies of Si- k_{α} (1.74 keV) and Sr- L_{α} (1.81 keV) are very close, only Ti- k_{α} (4.51 keV) and O- k_{α} (0.52 keV) were extracted from the EDS line profile and shown in Fig. 1(e). The interface between Si and SrTiO₃ is atomically and chemically sharp and free of oxide transition layers that are typically observed for oxides grown on Si (under different growth conditions). This is confirmed in the extracted oxygen and Ti EDS signals shown in Fig. 1(e), where the peaks drop sharply at the interface. Moreover, the Ti and oxygen EDS signals decrease towards the surface due to the wedge shaped of the sample but their ratio remains

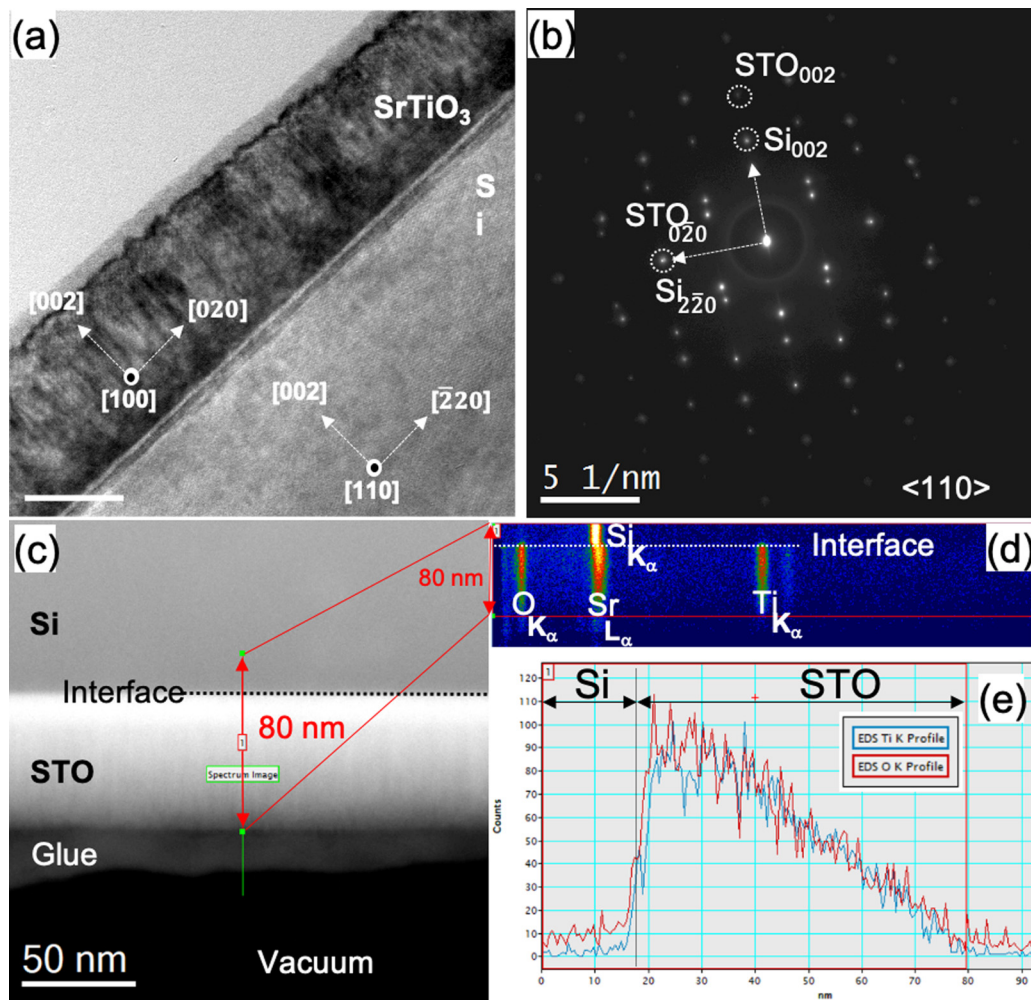


FIG. 1. (a) HRTEM image of the cross-section view, (b) SAED pattern of the SrTiO₃/Si interface oriented along the (110)//(100) zone axes. (c) HAADF-STEM, the line profile EDS spectrum is indicated. (d) EDS map spectrum obtained from the line as indicated in the HAADF-STEM image. (e) Extracted EDS signal of Ti and O from the EDS map spectrum. The black and white dashed lines on (c) and (d), respectively, mark the interface region and are aligned to each other.

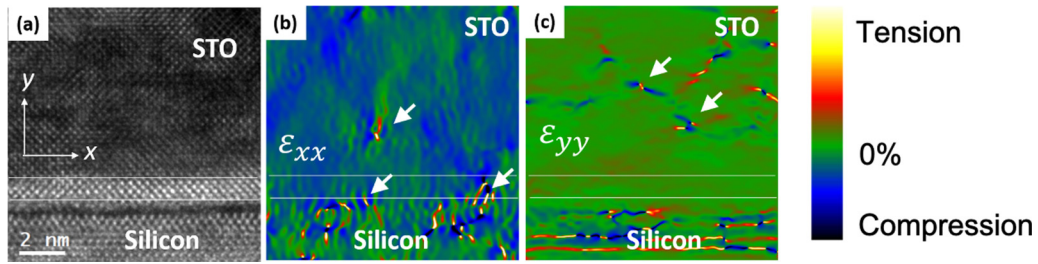


FIG. 2. (a) HRTEM image of SrTiO₃/Si, (b) in-plane and (c) out-of-plane strain maps of (a) using the GPA method. The bottom white line marks the interface between Si and SrTiO₃. The region between the two white lines is the interfacial SrTiO₃ region.

constant. Thus, within our signal accuracy, we do not observe oxygen loss as compared to Ti throughout the film thickness.

Strain analysis on the HRTEM image shown in Fig. 2(a) has been performed using the geometrical phase analysis (GPA) method [38]. The GPA method is a phase retrieval process from the HRTEM images using a pair of reflections of the reciprocal space. The reflections contain the amplitude (A_g) and phase (P_g) of a specific \mathbf{g}_{hkl} vector, where the phase is defined as the product between the \mathbf{g}_{hkl} vector and the displacement \mathbf{u}_x and \mathbf{u}_y directions. Subsequently, the strain maps in two dimensions are obtained by applying the sum of derivatives of the 2D displacements with respect to the x_i and x_j position. GPA generates color contours of strain directly mapping the location of relative strain in the HRTEM image. The \mathbf{g}_{020} and \mathbf{g}_{002} reflections from the SrTiO₃ film were used for the phase retrieval and strain maps, considering the x axis as the in-plane axis and the y axis as the out-of-plane axis. The coordinate references x - y are labeled in Fig. 2(a). The in-plane (ϵ_{xx}) and out-of-plane (ϵ_{yy}) strain maps are shown in Figs. 2(b) and 2(c), respectively. The strain determined by GPA is referenced to the SrTiO₃ relaxed crystal lattice, i.e., $a = 3.905 \text{ \AA}$. The sign of strain indicates whether the measured local lattice constant is larger (+, tensile strain) or smaller (−, compressive strain) than the lattice constant of bulk SrTiO₃. In Fig. 2, the bottom white line marks the interface between Si and SrTiO₃ and the top white line marks the SrTiO₃ region within 2 nm from the interface. The ϵ_{xx} strain map at the interfacial region indicates that SrTiO₃ is coherently strained in-plane to Si. The localized strain sites are continuous perpendicular to

the interface, continuing across the bottom white line marked on the image that delineates the interface from Si to SrTiO₃. The localized strain sites are mapped at the SrTiO₃/Si interface due to the lattice mismatch but are not propagated in the growth direction past 2 nm [Fig. 2(b)]. The color changes around the local sites in ϵ_{xx} show an inhomogeneous strain distribution directed along the growth direction [white arrows in Fig. 2(b)] signifying a strain gradient perpendicular to the interface. In comparison, the ϵ_{yy} strain map near the interface does not have a large color variation showing that the out-of-plane constant is more homogeneous. The ϵ_{yy} strain map shows some tensile strain denoted by the “red” regions. Past the interface, the strain relaxation shown by white arrows in Fig. 2(c) occurs more along the antiphase boundary domains and edge dislocations, the structural defects present in SrTiO₃ films on Si [21,39,40]. The color changes around the edge dislocations in ϵ_{xx} (white arrows) can be understood as insertion of an additional (001) plane. A change from compressive to tensile strain for the in-plane atoms ensues as the plane is inserted. The strain gradient in ϵ_{xx} is expected as the in-plane strain relaxes. Strain gradients induce polarization through the flexoelectric effect which becomes stronger as the size of the strain relaxation region becomes smaller.

The sheet resistance R_S increases as temperature decreases for both heterostructures as shown in Fig. 3(a). Below 30 K, the conductivity decreases logarithmically with T [Fig. 3(b)]. The slope of $\sigma(T)$ vs $\ln T$ (up to 20 K) is 1.11 ($K_{ee} = 0.11$, $F_0^\sigma = -0.42$) and 1.3 ($K_{ee} = 0.3$, $F_0^\sigma = -0.35$) for films A and B, respectively. The logarithmic behavior

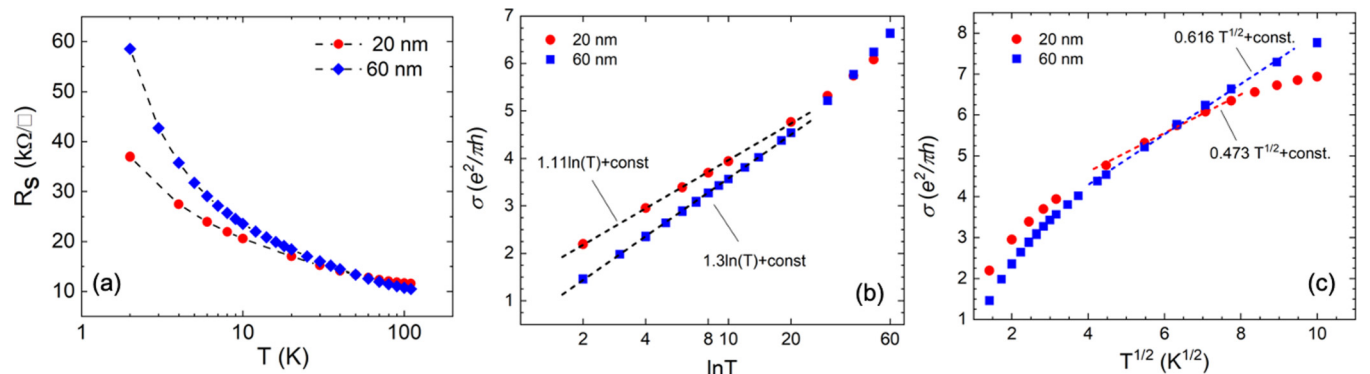


FIG. 3. (a) Sheet resistance for the 20-nm (circles) and 60-nm (squares) films versus temperature, (b) logarithmic temperature dependence of the conductivity along with the corresponding fits from 2 to 20 K, (c) conductivity versus the square root of temperature along with the corresponding fits from 20 to 60 K for the 20-nm film and from 20 to 80 K for the 60-nm film.

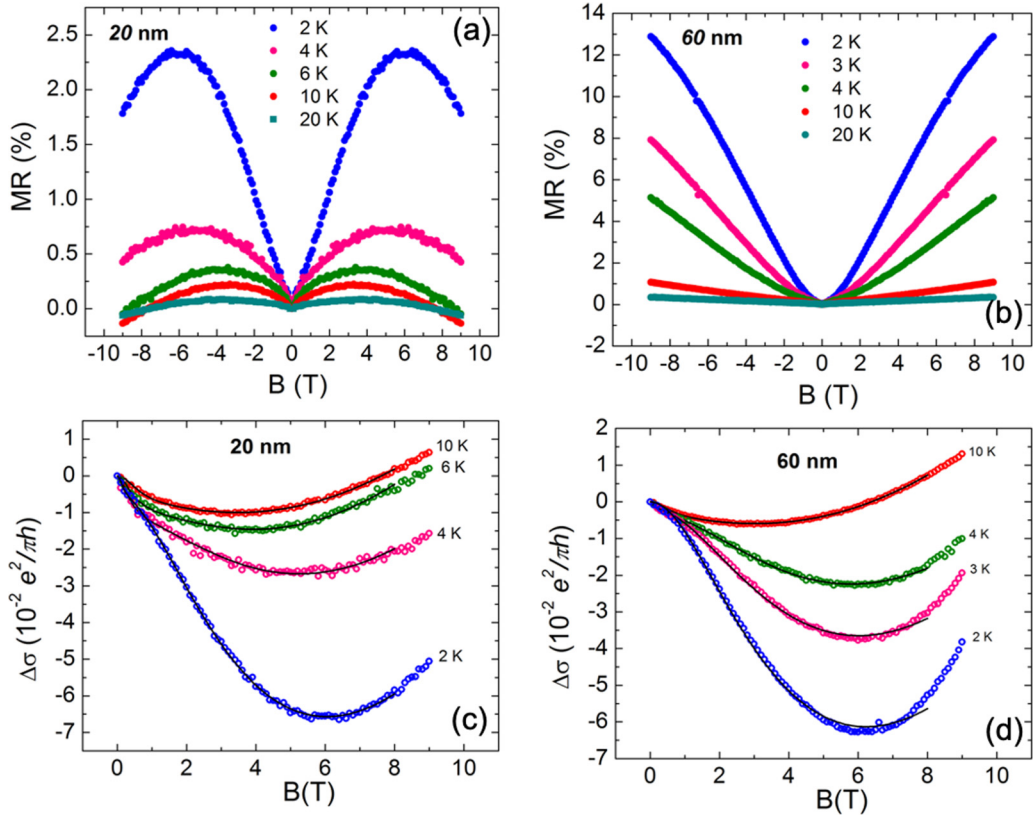


FIG. 4. Magnetoresistance (MR) for (a) the 20-nm film and (b) the 60-nm film. Magnetoconductance in units of $e^2/\pi h$ for (c) the 20-nm film and (d) for the 60-nm film after subtracting a parabolic background from the MR, the black lines show the fits (up to 8 T) to the HLN model including the Kohler term.

extends up to the same temperature for both films although their thicknesses differ by a factor of three establishing that below 20 K the electron system for both films is effectively 2D. Deviation from the logarithmic temperature dependence for temperatures above 20 K is evident for both films. We plot the measured conductivity against \sqrt{T} in Fig. 2(c) for temperatures up to 100 K. The temperature dependence of the conductivity changes from $\ln T$ to \sqrt{T} at 20 K and persists up to 60 K for the 20 nm film and up to 80 K for the 60 nm film as shown in Fig. 3(c). The slopes for these temperature ranges are $0.473 K^{-1/2}$ and $0.616 K^{-1/2}$ for the 20- and 60-nm films, respectively.

The measured conductivity at 100 K before the onset of quantum effects for each sample is $\sigma_D^A \cong 7 G_0$ and $\sigma_D^B \cong 8.4 G_0$. The corresponding sheet and volume carrier concentrations are: $n_s^A = 2 \times 10^{14} \text{ cm}^{-2}$ and, $n_s^B = 4.2 \times 10^{14} \text{ cm}^{-2}$, $n_V^A = 7.6 \times 10^{19} \text{ cm}^{-3}$, $n_V^B = 7 \times 10^{19} \text{ cm}^{-3}$. The diffusion constants calculated from the Drude conductivity (using 2D kinematic equations for the transport) are $D^A \sim 1.0 \text{ cm}^2/\text{s}$ and $D^B \sim 1.3 \text{ cm}^2/\text{s}$ while the elastic transport mean times are $\tau^A \approx 1.9 \text{ fs}$, $\tau^B \approx 1 \text{ fs}$. Our estimated mobility of $5 \text{ cm}^2/\text{Vs}$ at $\sim 100 \text{ K}$ is limited by longitudinal optic phonon scattering [41] and as such is not characteristic of the defectiveness of the films but rather of the phonon scattering. The mobility values are in agreement with published values for oxygen-deficient, Nb or La-doped SrTiO₃ crystals, which at temperatures between 100 and 200 K are $10\text{--}100 \text{ cm}^2/\text{Vs}$ $n_V = 4 \times 10^{15}\text{--}4 \times 10^{20} \text{ cm}^{-3}$ (roughly independent

from carrier concentration) [42,43]. The low temperature mobility cannot be determined from our conductivity data since quantum interference effects renormalize the mobility (through the scattering time).

The magnetoresistance (MR) (symmetrized in B with B applied perpendicular to the interface for the 20-nm film shown in Fig. 4(a) for several temperatures between 2 and 20 K, is nonmonotonic; it is positive at low B and becomes negative at high B resulting in the characteristic antilocalization maximum. The corresponding MC curve [Fig. 4(c)] has a minimum which becomes deeper and wider as the temperature decreases. This is consistent with the expected temperature evolution due to WAL [44] and indicates that τ_{so} is shorter than τ_ϕ [44–46]. Notably, the antilocalization minimum persists to temperatures above 20 K revealing a robust SOI. At 2 K the bare HLN expression fits the MC data well (two-parameters fit). At higher temperatures, the Kohler term improved the fittings considerably, and for temperatures above 14 K, the contribution of the Kohler term becomes comparable to that of HLN [47]. The fitting range (for all fits) extends to 8 T that encompasses the characteristic WAL minimum and is much smaller than the estimated $B_{\text{tr}} \approx 10^2\text{--}10^3 T$.

The MR of the 60-nm film [Fig. 4(b)] is positive and increases as the temperature decreases. The MR has a parabolic behavior at high temperatures [47]. A prominent cusp at low B that is typically associated with WAL gets more pronounced at low temperatures [47]. After subtracting a B^2 term from R_s , we obtain the residual resistance and the corresponding

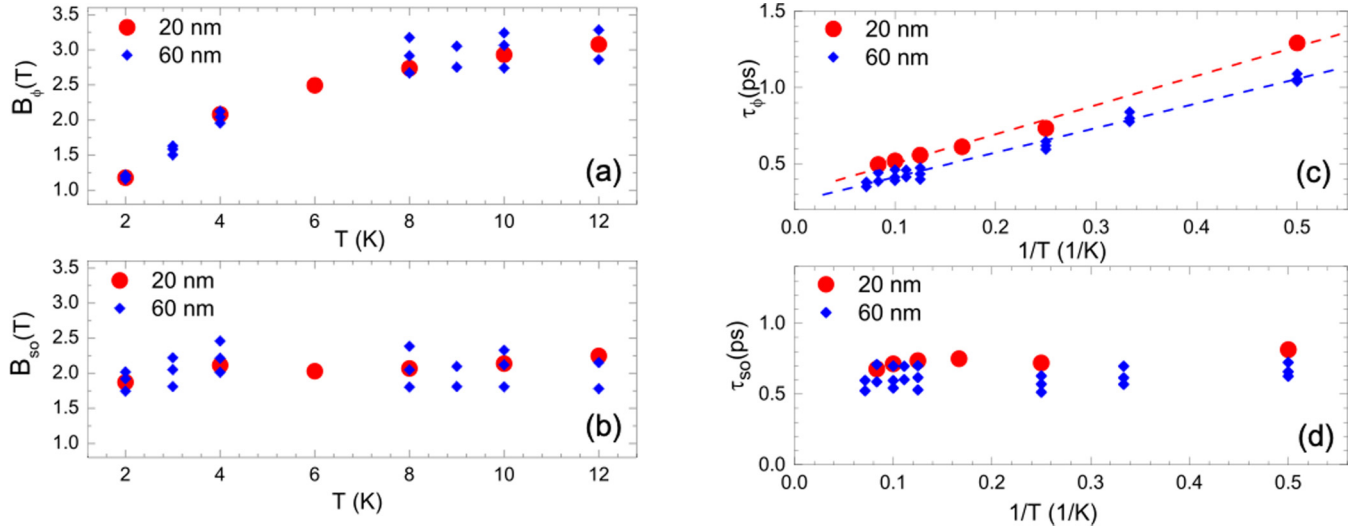


FIG. 5. Temperature dependence of the characteristic magnetic fields (a) B_ϕ and (b) B_{so} extracted from the HLN fits with the Kohler term for the 20-nm (red circles) and the 60-nm film (blue diamonds), (c) the phase-coherence time increasing linearly with $1/T$ and the corresponding linear fits to the data (dashed lines). (d) the spin-relaxation time is temperature-independent.

MC [Fig. 4(d)] [47], which shows the characteristic WAL minimum and closely resembles the MC of the 20-nm film. The MC of the 60-nm film is then fitted using the HLN expression and Kohler term as described previously for the 20-nm film. The extracted values of B_ϕ and B_{so} versus temperature are shown in Figs. 5(a) and 5(b). B_ϕ increases with T and is slightly larger for sample B than A. $B_{so} \cong 2$ T for both films and is roughly independent of temperature as expected for a degenerate electron system [44]. These B_{so} values are typical of those reported for WAL studies for the 2DES at SrTiO₃/LaAlO₃ [29,48]. At 2 K the corresponding lengths have similar values for both films $l_\phi \cong 12$ nm and $l_{so} \cong 9$ nm pointing to an intrinsic to the heterostructure origin for SOI. The corresponding τ_ϕ and τ_{so} are shown in Figs. 5(c) and 5(d) with τ_ϕ increasing linearly with $1/T$ as expected when the main phase breaking mechanism is EEI [24]. Unlike τ_ϕ , τ_{so} is temperature-independent and is larger for film A with the lower n_s . This is consistent with the Dyakonov-Perel spin relaxation mechanism where τ_{so} decreases with n_s [49].

The transverse resistance R_{xy} is linear in B [Fig. 6(a)]. The Hall coefficient R_H is negative and as the temperature decreases, R_H increases in magnitude and, accordingly, the sheet carrier density $n_s = 1/eR_H$ appears to decrease [Fig. 6(b)]. Film B has a higher carrier concentration, $n_s^B \cong 3 \times 10^{14} \text{ cm}^{-2}$ than A, $n_s^A \cong 1.5 \times 10^{14} \text{ cm}^{-2}$. Additionally, n_s^B decreases faster with temperature than n_s^A . At first glance, we might attribute this apparent decrease of n_s with temperature to a freeze-out of charge carriers where electrons trapped by defects get activated to conduction as temperature increases ($n_s \propto e^{-E_A/k_B T}$), often observed in SrTiO₃ SrTiO₃-based systems [50–53]. This is not the case here since n_s decreases logarithmically with temperature as shown in Fig. 6(b) following the temperature dependence of $\delta\sigma_{EEI}(T)$. In contrast, we show that the apparent decrease of n_s is, in fact, caused by the EEI correction to R_H . The change in the Hall coefficient, $[R_H(T) - R_H(20 \text{ K})]/R_H(20 \text{ K}) = \Delta R_H/R_H = \delta R_H/R_H$ along with $\frac{\delta\sigma_{EEI}}{\sigma_d}$ calculated using Eq. (1) are plotted as a function of temperature in Fig. 6(c). The

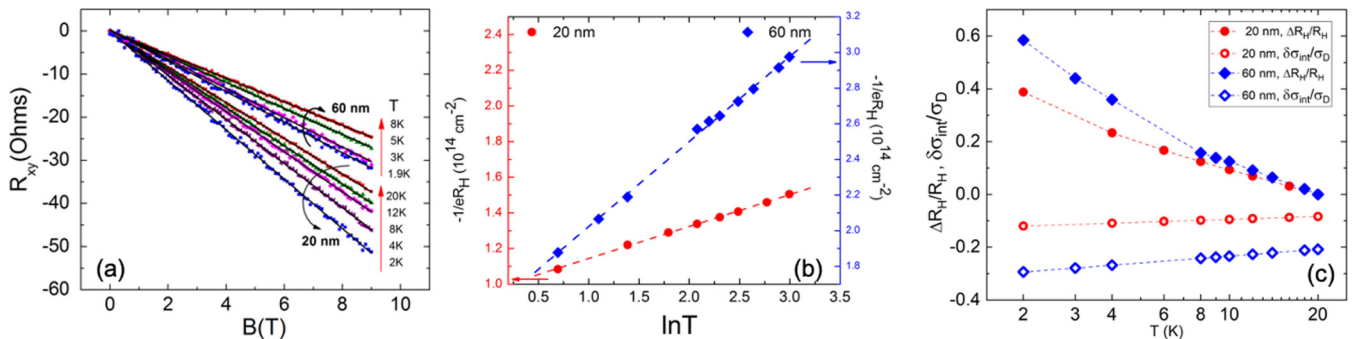


FIG. 6. (a) Hall resistance for several temperatures between 2 and 20 K for both samples, (b) logarithmic temperature dependence of the inverse Hall coefficient along with linear fits to the data, (c) relative change of the Hall coefficient from 20 K $[R_H(T) - R_H(20 \text{ K})]/R_H(20 \text{ K}) = \Delta R_H/R_H(20 \text{ K})$ (closed symbols) and interaction correction to the conductivity over the Drude conductance $\frac{\delta\sigma_{EEI}}{\sigma_d}$ (open symbols) vs $\ln T$ for both samples following the predicted $\frac{(\delta R_H)_{EEI}}{R_H} = -2 \frac{\delta\sigma_{EEI}}{\sigma_d}$ relation for interaction effects (the lines are a guide to the eye).

logarithmic increase of $\Delta R_H/R_H$ with decreasing temperature agrees with theoretical predictions and the ratio of the two quantities indeed approaches -2 as $T \rightarrow 0$ [24]. As a result, EEI effects determine the temperature dependence of $1/eR_H$, which therefore does not correspond to the net carrier concentration. Electronic correlations, in addition to disorder, cause the apparent electron localization. EEI and quantum interference effects renormalize the carrier concentration and scattering time (and hence mobility), respectively, driving the system to an insulating state.

The spin splitting energy calculated using $\Delta = \hbar\Omega_3$, with $\Omega_3^2 = 1/(2\tau\tau_{so})$ is $\Delta^A \cong 12$ meV and $\Delta^B \cong 19$ meV. These energies are more than 10 times larger than the lowest temperature in our experiments and they are also larger than the reported spin splitting energies of 0.5 meV on the gated SrTiO₃ surface [7] and ≈ 2 –5, meV for SrTiO₃-based systems [54,55]. These estimated spin splitting energies are comparable to those observed on gated SrTiO₃/LaAlO₃ [6] for a gate voltage of 100 V even though no gating is applied here. We have not observed SOI for SrTiO₃/Si heterostructures that have thicknesses and conductivities similar to the 20-nm and 60-nm films presented in this work but smaller carrier concentrations ($\sim 10^{13}$ cm⁻²) and higher disorder. This indicates that the observed SOI is not solely due to disorder and is likely related to band filling and the orbital structure of SrTiO₃.

The 2D electronic behavior from the magnetotransport results and analysis necessitates electron confinement within SrTiO₃ for both films. The effective dimensionality of the system is the number of dimensions for which the system is larger than the characteristic length scale. For interference effects, the characteristic length is the phase coherence length l_ϕ while for EEI, the characteristic length is the thermal length $l_T = \sqrt{\hbar D/k_B T}$ [23]. At 2 K, the phase coherence length is $l_\phi \approx 12$ nm for both films, which is smaller than the actual film thicknesses so the carriers should be confined within an effective thickness d_o . As temperature increases, both l_T and l_ϕ decrease and at a characteristic temperature, there should be a crossover from 2D to 3D behavior manifested as a deviation of the conductance from the $\ln T$ dependence to \sqrt{T} dependence. As noted earlier, this crossover occurs around 20 K for both films indicating that the effective 2DES thickness d_o is similar for the two films despite the difference in their physical thickness. Taking the 3D to 2D crossover to occur when $l_{\phi,T} \sim 2d_o$ [27], and from the estimated $l_{\phi,T} \approx 6$ –7 nm at 20 K, the upper limit for the effective thickness is $d_o \approx 3$ –4 nm comparable to the thickness of the strained SrTiO₃ layer. Above the crossover temperature, the electrons are no longer confined within a thickness of $l_{\phi,T}$ ($l_{\phi,T} \lesssim 2d_o$) and the electronic behavior for interference and EEI effects becomes 3D.

Moreover, an effective thickness of $d_o \approx 4$ nm indicates that the volume carrier densities are much larger than the calculated ones when assuming that the electrons are distributed throughout the total film thickness and they are on the order of $\sim 10^{21}$ cm⁻³ nearing the electron density required for a strongly correlated Mott insulator $\sim 1.7 \times 10^{22}$ cm⁻³. Such high carrier concentrations are not easily achieved in SrTiO₃-based systems even under electrostatic gating. In contrast, in the SrTiO₃/Si system carrier concentrations $\sim 10^{14}$ cm⁻²

occur spontaneously (without gating) and are confined within 4 nm. Since strong SOI and confinement at these high carrier concentrations have not been observed on the bare or gated SrTiO₃ surface, we assume that the 2DES is confined at the interface with Si. This points directly to a confinement potential near the interface. In the absence of a confining potential, electrons originating from oxygen vacancies, which are uniformly distributed in our films, as evidenced from the EDS line profile [Fig. 1(e)], should also be uniformly distributed throughout the SrTiO₃ film. A large electric field at the interface would cause electrons distributed throughout the film thickness to accumulate at the interface accounting for the confinement of these large carrier densities. Such an electric field could be induced by strain or band offsets.

In the SrTiO₃/Si system, strain causes splitting of the t_{2g} levels with the d_{xy} band lower in energy than the elliptical d_{xz}/d_{yz} bands [56]. Strain and strain gradients also break the structure inversion symmetry of SrTiO₃ and could induce SOI [49,57]. Strain at the interface may also account for the observed SOI. The inhomogeneous strain distribution in ϵ_{xx} directed along the growth direction produces a strain gradient that could induce polarization at the interface through the flexoelectric effect. SrTiO₃ has a large flexoelectric coefficient. In bulk single-crystal SrTiO₃, the flexoelectric coefficient was measured by directly applying a static force and bending the crystal; along the (001) directions, the value of the flexoelectric response was ~ 6 C/nm producing local polarization of several $\mu\text{C}/\text{cm}^{-2}$, which increases as temperature decreases [58]. In another recent experiment, the flexoelectric polarization in SrTiO₃ core dislocations measured using STEM was $\sim 28 \mu\text{C}/\text{cm}^{-2}$ [59]. This polarization corresponds to $\sim 1.8 \times 10^{14}$ cm⁻², which is in-line with the measured carrier concentrations here. The induced flexoelectric polarization would further require compensation by either screening through free carrier redistribution or accumulation of defects such as oxygen vacancies near the interface. Lattice strain has been shown to affect the vacancy formation energy of several metal-oxide materials although compressive strain, as in the case of the SrTiO₃/Si system, hinders vacancy formation, and tensile strain favors oxygen vacancies [60]. Subsequent measurements using off-axis electron holography are required to map the electrostatic potentials and the distribution of the electric field in the Si/SrTiO₃ heterojunction.

Another possibility is that a built-in electric field at the interface is caused by the band offsets between Si and SrTiO₃. Until recently, the SrTiO₃/Si heterojunction was believed to be a type-II heterojunction with a very small conduction band offset [15]. It was recently reported that the band arrangement of this heterojunction can be altered with carrier density; it can become type-III with a conduction band offset of 2.7–3.3 eV for Nb-doped SrTiO₃ on Si(001) [16]. It was shown that the SrTiO₃ band bending creates a potential well of ~ 2 V confining the carriers to a few nanometers in the out-of-plane direction and a high-density electron gas was predicted to arise near the interface [16]. This built-in field can also cause carrier confinement and a Rashba-SOI as in conventional III-V semiconductor heterostructures [44]. Subsequent field-gating experiments could elucidate the origin of the observed SOI.

IV. CONCLUSION

Employing the established analysis framework for 2D quantum systems such as GaAs-based quantum wells to understand the electronic properties of the SrTiO₃/Si heterostructure allows us to evaluate the SOI rigorously but also allows us to deconvolute and extract the contributions of EEI to transport that are not typically considered for SrTiO₃-based systems. The extracted F_0^σ values suggest that EEI are repulsive and are stronger for the film with higher n_s . In strongly correlated electron systems, as n_s (band filling) increases, electron occupation in a unit cell increases, enhancing electron correlations. The combination of repulsive EEI at large electron densities and structural distortions—due to strain and the antiferrodistortive transition at ~ 105 K—is consistent with a predicted Mott transition in SrTiO₃ [61]. Additionally, in SrTiO₃-based systems, interaction effects are predicted to be interorbital. They arise from electronic correlations between the populated d_{xy} and d_{yz}/d_{zx} bands that are also mixed by SOI [62]. It has been reported that electronic interactions cause a competition between the occupancies of different bands such that when the population of one band increases, the energies of the states in the other band are shifted and the other band's occupation decreases. In the presence of such a competition, occupying the band with the highest single-particle density of states is usually preferable, as this results in lower single-particle energy [63]. When multiple bands are occupied, a

nonlinear Hall effect is typically observed due to two-carrier transport, i.e., different-mobility electrons originating from two different bands [63,64]. In our case, the Hall effect is linear in B (within the accuracy of the experiment). Though multiple bands of SrTiO₃ may be occupied, the electrons participating in the electronic transport appear to be originating from bands with comparable mobilities or from a single band possibly due to EEI. Some evidence for multiorbital effects (presence of additional high mobility carriers) is provided by the MC_{Khl} term and the B^2 background in the MR of the 60-nm film.

We, hereby, report the simultaneous observation of large spin-splitting without field gating, 2D confinement, and EEI in a chemically abrupt SrTiO₃/Si heterojunction. The integration of oxides with semiconductors remains important for the technological advancement of the next generation electronics that use oxide functionalities and may be achieved by conceiving and implementing new device paradigms. Observing concomitant SOI and EEI in SrTiO₃ integrated directly on Si could broaden the device applications of the most advanced and mature semiconductor technology.

ACKNOWLEDGMENT

This project was supported by NSF-CAREER Award No. DMR-1255629 and by DOD Grant No. W911NF-18-1-0439.

-
- [1] Y. A. Bychkov and E. I. Rashba, *J. Phys. C* **17**, 6039 (1984).
- [2] B. Habib, J. Shabani, E. P. De Poortere, M. Shayegan, and R. Winkler, *Phys. Rev. B* **75**, 153304 (2007).
- [3] G. Khalsa and A. H. MacDonald, *Phys. Rev. B* **86**, 125121 (2012).
- [4] G. Jackeli and G. Khaliullin, *Phys. Rev. Lett.* **101**, 216804 (2008).
- [5] N. Yamaguchi and F. Ishii, *e-J. Surf. Sci. Nanotechnol.* **16**, 360 (2018).
- [6] A. D. Caviglia, M. Gabay, S. Gariglio, N. Reyren, C. Cancellieri, and J. M. Triscone, *Phys. Rev. Lett.* **104**, 126803 (2010).
- [7] H. Nakamura, T. Koga, and T. Kimura, *Phys. Rev. Lett.* **108**, 206601 (2012).
- [8] Z. C. Zhong, A. Toth, and K. Held, *Phys. Rev. B* **87**, 161102 (2013).
- [9] A. F. Santander-Syro, O. Copie, T. Kondo, F. Fortuna, S. Pailhes, R. Weht, X. G. Qiu, F. Bertran, A. Nicolaou, A. Taleb-Ibrahimi *et al.*, *Nature (London)* **469**, 189 (2011).
- [10] W. Meevasana, P. D. C. King, R. H. He, S. K. Mo, M. Hashimoto, A. Tamai, P. Songsiririthigul, F. Baumberger, and Z. X. Shen, *Nat. Mater.* **10**, 114 (2011).
- [11] P. D. C. King, S. M. Walker, A. Tamai, A. de la Torre, T. Eknapakul, P. Buaphet, S. K. Mo, W. Meevasana, M. S. Bahramy, and F. Baumberger, *Nat. Commun.* **5**, 3414 (2014).
- [12] G. Khalsa, B. Lee, and A. H. MacDonald, *Phys. Rev. B* **88**, 041302 (2013).
- [13] K. V. Shanavas, *Phys. Rev. B* **93**, 045108 (2016).
- [14] Y. Kim, R. M. Lutchyn, and C. Nayak, *Phys. Rev. B* **87**, 245121 (2013).
- [15] S. A. Chambers, Y. Liang, Z. Yu, R. Droopad, and J. Ramdani, *J. Vac. Sci. Technol. A* **19**, 934 (2001).
- [16] Z. H. Lim, N. F. Quackenbush, A. N. Penn, M. Chrysler, M. Bowden, Z. Zhu, J. M. Ablett, T. L. Lee, J. M. LeBeau, J. C. Woicik *et al.*, *Phys. Rev. Lett.* **123**, 026805 (2019).
- [17] S. H. Baek and C. B. Eom, *Acta Mater.* **61**, 2734 (2013).
- [18] Z. Yu, Y. Liang, C. Overgaard, X. Hu, J. Curless, H. Li, Y. Wei, B. Craigo, D. Jordan, R. Droopad *et al.*, *Thin Solid Films* **462**, 51 (2004).
- [19] R. J. Cottier, N. A. Steinle, D. A. Currie, and N. Theodoropoulou, *Appl. Phys. Lett.* **107**, 221601 (2015).
- [20] F. S. Aguirre-Tostado, A. Herrera-Gomez, J. C. Woicik, R. Droopad, Z. Yu, D. G. Schlom, P. Zschack, E. Karapetrova, P. Pianetta, and C. S. Hellberg, *Phys. Rev. B* **70**, 201403 (2004).
- [21] M. P. Warusawithana, C. Cen, C. R. Sleasman, J. C. Woicik, Y. Li, L. F. Kourkoutis, J. A. Klug, H. Li, P. Ryan, L.-P. Wang *et al.*, *Science* **324**, 367 (2009).
- [22] J. C. Woicik, H. Li, P. Zschack, E. Karapetrova, P. Ryan, C. R. Ashman, and C. S. Hellberg, *Phys. Rev. B* **73**, 024112 (2006).
- [23] T. Ando, A. B. Fowler, and F. Stern, *Rev. Mod. Phys.* **54**, 437 (1982).
- [24] B. L. Altshuler and A. G. Aronov, *Electron-Electron Interactions in Disordered Systems*, Modern Problems in Condensed Matter Physics (Elsevier, Amsterdam, 1985).
- [25] Y. J. Chang, A. Bostwick, Y. S. Kim, K. Horn, and E. Rotenberg, *Phys. Rev. B* **81**, 235109 (2010).

- [26] H. Uwe, R. Yoshizaki, T. Sakudo, A. Izumi, and T. Uzunaki, *Jpn. J. Appl. Phys.* **24**, 335 (1985).
- [27] P. A. Lee and T. V. Ramakrishnan, *Rev. Mod. Phys.* **57**, 287 (1985).
- [28] S. V. Iordanskii, Y. B. Lyandageller, and G. E. Pikus, *JETP Lett.* **60**, 206 (1994).
- [29] H. X. Liang, L. Cheng, L. M. Wei, Z. L. Luo, G. L. Yu, C. G. Zeng, and Z. Y. Zhang, *Phys. Rev. B* **92**, 075309 (2015).
- [30] D. Rainer and G. Bergmann, *Phys. Rev. B* **32**, 3522 (1985).
- [31] G. Zala, B. N. Narozhny, and I. L. Aleiner, *Phys. Rev. B* **64**, 214204 (2001).
- [32] G. Zala, B. N. Narozhny, and I. L. Aleiner, *Phys. Rev. B* **64**, 201201 (2001).
- [33] G. Zala, B. N. Narozhny, and I. L. Aleiner, *Phys. Rev. B* **65**, 020201 (2002).
- [34] H. Li, X. Hu, Y. Wei, Z. Yu, X. Zhang, R. Droopad, A. A. Demkov, J. Edwards, K. Moore, W. Ooms *et al.*, *J. Appl. Phys.* **93**, 4521 (2003).
- [35] C. Capan, G. Y. Sun, M. E. Bowden, and S. A. Chambers, *Appl. Phys. Lett.* **100**, 052106 (2012).
- [36] A. B. Posadas, K. J. Kormondy, W. Guo, P. Ponath, J. Geler-Kremer, T. Hadamek, and A. A. Demkov, *J. Appl. Phys.* **121**, 105302 (2017).
- [37] S. M. Sze and M. K. Lee, *Semiconductor Devices, Physics, and Technology*, 3rd ed (Wiley, Hoboken, NJ, 2012).
- [38] M. J. Hytch, E. Snoeck, and R. Kilaas, *Ultramicroscopy* **74**, 131 (1998).
- [39] G. Y. Yang, J. M. Finder, J. Wang, Z. L. Wang, Z. Yu, J. Ramdani, R. Droopad, K. W. Eisenbeiser, and R. Ramesh, *J. Mater. Res.* **17**, 204 (2002).
- [40] H. W. Wu, T. Aoki, A. B. Posadas, A. A. Demkov, and D. J. Smith, *Appl. Phys. Lett.* **108**, 091605 (2016).
- [41] H. P. Frederikse and W. R. Hosler, *Phys. Rev.* **161**, 822 (1967).
- [42] A. Spinelli, M. A. Torija, C. Liu, C. Jan, and C. Leighton, *Phys. Rev. B* **81**, 155110 (2010).
- [43] A. Verma, A. P. Kajdos, T. A. Cain, S. Stemmer, and D. Jena, *Phys. Rev. Lett.* **112**, 216601 (2014).
- [44] G. M. Minkov, A. A. Sherstobitov, A. V. Germanenko, O. E. Rut, V. A. Larionova, and B. N. Zvonkov, *Phys. Rev. B* **71**, 165312 (2005).
- [45] M. I. Dyakonov and V. I. Perel, *Sov. Phys. Solid State* **13**, 3023 (1972).
- [46] M. I. Dyakonov, in *Spin Physics in Semiconductors*, Springer Series in Solid State Sciences (Springer, Berlin, 2008), p. 157.
- [47] See Supplemental Material at <http://link.aps.org/supplemental/10.1103/PhysRevB.102.125423> for details on the magnetotransport analysis.
- [48] G. Herranz, G. Singh, N. Bergeal, A. Jouan, J. Lesueur, J. Gazquez, M. Varela, M. Scigaj, N. Dix, F. Sanchez *et al.*, *Nat. Commun.* **6**, 6028 (2015).
- [49] R. Moriya, K. Sawano, Y. Hoshi, S. Masubuchi, Y. Shiraki, A. Wild, C. Neumann, G. Abstreiter, D. Bougeard, T. Koga *et al.*, *Phys. Rev. Lett.* **113**, 086601 (2014).
- [50] M. Huijben, G. Rijnders, D. H. A. Blank, S. Bals, S. Van Aert, J. Verbeeck, G. Van Tendeloo, A. Brinkman, and H. Hilgenkamp, *Nat. Mater.* **5**, 556 (2006).
- [51] Z. Q. Liu, D. P. Leusink, X. Wang, W. M. Lu, K. Gopinadhan, A. Annadi, Y. L. Zhao, X. H. Huang, S. W. Zeng, Z. Huang *et al.*, *Phys. Rev. Lett.* **107**, 146802 (2011).
- [52] V. K. Guduru, A. McCollam, A. Jost, S. Wenderich, H. Hilgenkamp, J. C. Maan, A. Brinkman, and U. Zeitler, *Phys. Rev. B* **88**, 241301 (2013).
- [53] M. Huijben, G. W. J. Hassink, M. P. Stehno, Z. L. Liao, G. Rijnders, A. Brinkman, and G. Koster, *Phys. Rev. B* **96**, 075310 (2017).
- [54] Y. Y. Pai, A. Tylan-Tyler, P. Irvin, and J. Levy, *Rep. Prog. Phys.* **81**, 036503 (2018).
- [55] W. N. Lin, L. Li, F. Dogan, C. J. Li, H. Rote, X. J. Yu, B. M. Zhang, Y. Y. Li, W. S. Lew, S. J. Wang *et al.*, *Nat. Commun.* **10**, 3052 (2019).
- [56] J. C. Woicik, E. L. Shirley, C. S. Hellberg, K. E. Andersen, S. Sambasivan, D. A. Fischer, B. D. Chapman, E. A. Stern, P. Ryan, D. L. Ederer *et al.*, *Phys. Rev. B* **75**, 140103 (2007).
- [57] Y. Kato, R. C. Myers, A. C. Gossard, and D. D. Awschalom, *Nature (London)* **427**, 50 (2004).
- [58] P. Zubko, G. Catalan, A. Buckley, P. R. L. Welche, and J. F. Scott, *Phys. Rev. Lett.* **99**, 167601 (2007).
- [59] P. Gao, S. Z. Yang, R. Ishikawa, N. Li, B. Feng, A. Kumamoto, N. Shibata, P. Yu, and Y. Ikuhara, *Phys. Rev. Lett.* **120**, 267601 (2018).
- [60] D. Marrocchelli, L. X. Sun, and B. Yildiz, *J. Am. Chem. Soc.* **137**, 4735 (2015).
- [61] J. R. Tolsma, M. Polini, and A. H. MacDonald, *Phys. Rev. B* **95**, 205101 (2017).
- [62] E. Maniv, M. Ben Shalom, A. Ron, M. Mograbi, A. Palevski, M. Goldstein, and Y. Dagan, *Nat. Commun.* **6**, 8239 (2015).
- [63] A. E. M. Smink, M. P. Stehno, J. C. de Boer, A. Brinkman, W. G. van der Wiel, and H. Hilgenkamp, *Phys. Rev. B* **97**, 245113 (2018).
- [64] F. Gunkel, C. Bell, H. Inoue, B. Kim, A. G. Swartz, T. A. Merz, Y. Hikita, S. Harashima, H. K. Sato, M. Minohara *et al.*, *Phys. Rev. X* **6**, 031035 (2016).